JOURNAL OF GEOPHYSICAL RESEARCH, VOL. 106, NO. C7, PAGES 14,015–14,034, JULY 15, 2001

An *s* coordinate density evolving model of the northwest European continental shelf
1, Model description and density structure

Jason T. Holt and Ian D. James

Proudman Oceanographic Laboratory, Bidston Observatory, Birkenhead, United Kingdom

Abstract. The Proudman Oceanographic Laboratory Three-Dimensional Baroclinic B grid model (POL3DB) has been developed to incorporate features suitable for the modeling of baroclinic processes on the shelf, at the shelf slope, and in ocean regions to allow long-term coupled ocean-shelf simulations. We test the model on the northwest European continental shelf in the period November 1988 to October 1989 against satellite sea surface temperature measurements, against CTD sections both on and off the shelf, and (in summary) against the whole of the North Sea Project CTD data set. The model accurately reproduces the seasonal cycle in the shelf-wide spatial temperature structure seen in the observations. Spatial correlations range from r=0.92 in December to 0.79 in July, and the overall rms errors range from 0.8°C in April to 1.6°C in July. We demonstrate that the increase in the errors during the summer is due to uncertainties in modeling the vertical temperature structure. Compared with a climatology, the large-scale sea surface salinity structure is also well modeled ($r = 0.80$), but there is a tendency for the model to overestimate the salinity in the Norwegian Trench and underestimate it in the Kattegat. The *s* coordinates (a modified sigma-coordinate system) allow the formation of a seasonal mixed layer across the shelf break and into the northeast Atlantic with a modest vertical resolution. The accuracy to which this deep water region is modeled is limited by the initial and boundary conditions and by the extent of the model domain.

1. Introduction

The simulation of seasonal currents, water quality parameters, and plankton variability in shelf seas requires a physical model which goes beyond the well-established tide and surge models [e.g., *Flather et al.*, 1991; *Kwong et al.*, 1997] to include the effects of horizontal and vertical density variations. This is necessary since the former introduces seasonal transports not seen in the constant density models while the latter controls the vertical fluxes crucial to biological production. Moreover, thermal fronts affect both the horizontal and vertical transport of tracers. To this end, a three-dimensional model with temperature and salinity treated as prognostic variables has been developed: the Proudman Oceanographic Laboratory Three-Dimensional Baroclinic B grid model (POL3DB). The origins of this model lie with *James* [1986], and it has subsequently been developed [*James*, 1996] to include a sophisticated advection scheme, the "Piecewise Parabolic Method" (PPM) described below. This has excellent feature preserving properties making it ideal for the simulation of on-shelf baroclinic features such as river plumes [*James*, 1997] and fronts [*Proctor and James*, 1996] and the transport of tracers from localized sources [*Holt and James*, 1999a]. Moreover, the model is formulated on an *Arakawa* [1972] B grid (see section 3.1), in contrast to the C grid used in many shelf sea models, for example, the Princeton Ocean Model (POM) [*Blumberg and Mellor*, 1987]. The B grid is more commonly used in deep ocean models [e.g., *Killworth et al.*, 1991] and is well suited to the modeling of horizontal density variations since the Coriolis term can be calculated without averaging. This helps prevent the dispersion of the velocity features associated with fronts, in contrast with the C grid which requires averaging over a number of points to calculate this term. The downside is that continuity and scalar advection require averaging of velocities not required on the C grid. It is this choice of grid and the nondiffusive advection that particularly distinguishes this model.

The objective of this work is to make a comprehensive simulation of the physical oceanography of the northwest European continental shelf over the period of a year and to critically compare this with the available observations. This paper focuses on the large-scale horizontal temperature and salinity variations and their stratification. Published alongside this [*Holt et al.*, this issue], and referred to as HJJ in this work, is an account of the tidal currents and elevations and the residual currents on timescales of weeks to months.

We model the domain shown in Figure 1 (along with the bathymetry) on a $\sim$ 12 km finite difference grid (described in section 3.1). This region matches that of the POL two-

Paper number 2000JC000304.
0148-0227/01/2000JC000304$09.00

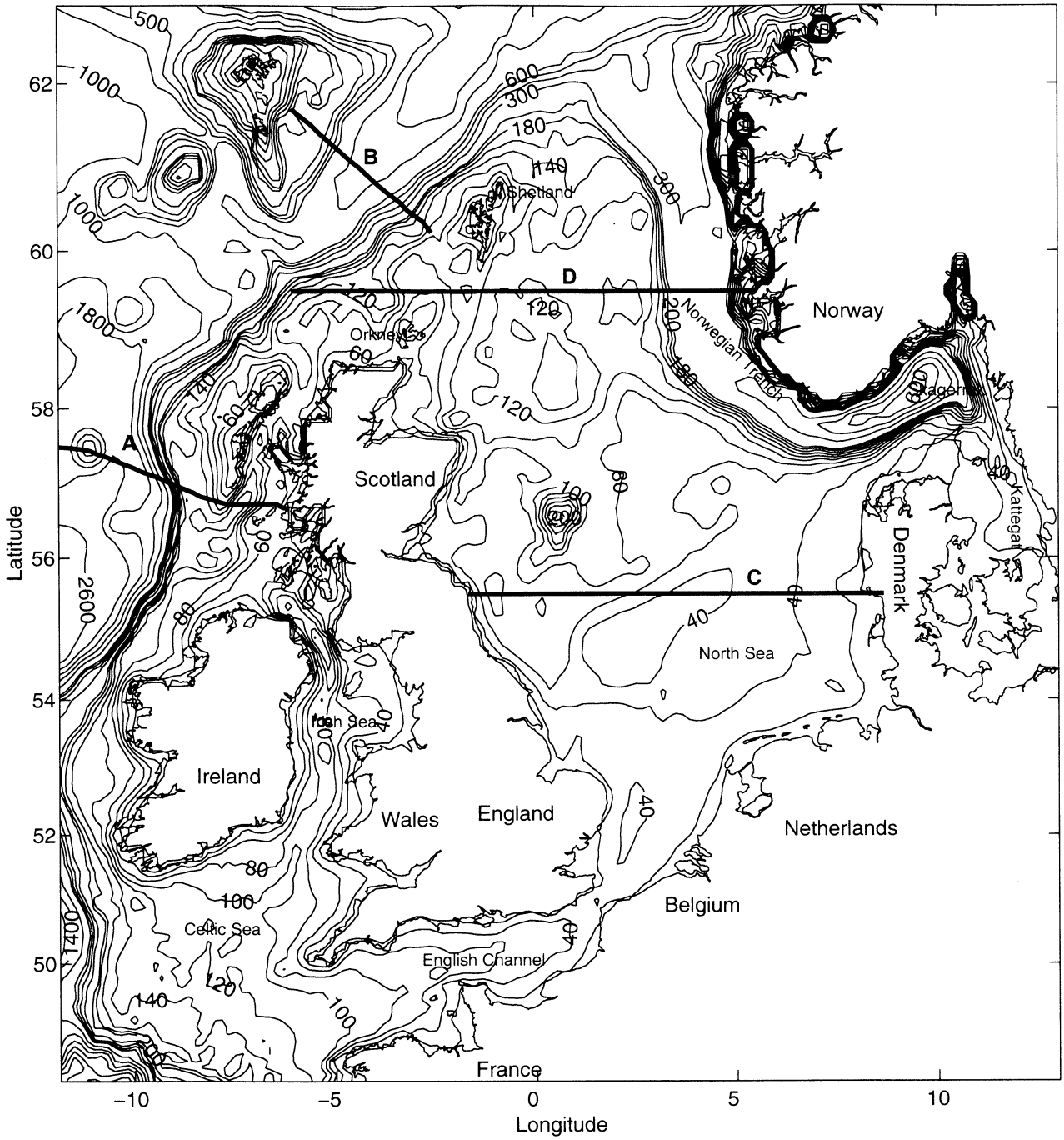

Figure 1. Model Bathymetry. The contour interval is 20 m for $20 < H < 200$ m; 100 m for $200 < H < 600$ m; and 400 m for $600 < H < 4000$ m. Also shown are the four CTD sections used for comparison with the model data.

dimensional model used for operational tide and surge forecasting by the U.K. Meteorological Office and a more recent three-dimensional model [*Kwong et al.*, 1997]. The region of this model was initially dictated by the availability of forcing data but is far from ideal particularly at the southern and western boundaries where the open boundary crosses the shelf break at three locations. The present work focuses on the dynamics on the shelf: however, the domain includes large areas with water depth >200 m intimately connected with the shallow water regions. For example, the Norwegian Trench provides the major transport pathway out of the North Sea. Moreover, this work is a precursor to extending the model domain west to 20°W, north to 65°N, and south to 40°N, hence including a large area of the northeast Atlantic. Therefore we have included in the formulation of this model a number of techniques pertinent to the treatment of deep water. Although the model equations remain in σ coordinates in the vertical, the spacing of these coordi-

nate surfaces on the finite difference grid is allowed to vary in the horizontal according to the s coordinate transform of *Song and Haidvogel* [1994] (see section 3.1); the pressure gradient calculations are made by interpolation onto horizontal planes through the points where velocities are defined (section 3.4), and a term for the variation of compressibility with temperature and salinity (section 2.1) is included in the model equation of state for sea water. It is not our intention to discuss the full implications of these techniques in this paper as they each deserve a more detailed account than can be given here; this will be presented elsewhere. As in previous applications, the model does not include horizontal diffusion, since it is not needed for model stability.

There have been a number of previous numerical simulations of the northwest European shelf with prognostic temperature and/or salinity. These have primarily used either POM [e.g., *Oey and Chen*, 1992b] or the Institut für Meereskunde Hamburg model of *Backhaus and Hainbucher* [1987] [e.g., *Pohlmann*, 1996]. In these two examples the surface forcing was constrained either by relaxation to climatology or by using surface temperature observations as a boundary condition. In the present work we adopt a similar approach to *Holt and James* [1999b] and allow the model to evolve with a minimum of constraints: only the open boundary temperature and salinity is relaxed to climatology. This permits an unbiased comparison with satellite sea surface temperature (SST) measurements.

The resolution of this model lies between that used in the previous shelf-wide studies ($\sim$ 20 km [*Oey and Chen*, 1992b] and $\sim$ 25 km [*Pohlmann*, 1996]) and in studies of limited areas of the North Sea ($\sim$ 4 km in the Norwegian Trench [*Oey and Chen*, 1992a] and $\sim$ 2.5 km in the German Bight [*Schrum*, 1997] and the southern North Sea [*Proctor and James*, 1996]). The internal Rossby radius in this domain might be expected to range from $\sim$ 3 km in the river plumes [*de Kok*, 1997] to 10-20km in the Norwegian Trench to $\sim$ 30 km in the northeast Atlantic. Hence this model would not be expected to resolve the details of the on-shelf baroclinic features (such as frontal instabilities and river plumes), but we might hope that it would simulate their overall characteristics (such as the frontal locations) more accurately than the previous coarser resolution studies. In the Norwegian Trench and northeast Atlantic the model is eddy permitting; however, a study in the Faeroe-Shetland Channel [*Oey*, 1997] showed that convergence of the eddy energetics required a resolution of <2 km and eddies in the Norwegian Trench might require a finer resolution. So even in these deep, highly stratified regions, the present resolution is unlikely to accurately model the details of the baroclinic features.

In sections 2 and 3 we present a complete description of the POL3DB model as applied to the northwest European Continental shelf. This summarizes the descriptions given by *Proctor and James* [1996], *James* [1996], and *Holt and James* [1999b], with a number of modifications particular to this context. The sea surface temperature and salinity structure is discussed in section 4, and the stratification is discussed in section 5.

2. Model Description: Model Equations

The model is formulated in spherical polar sigma coordinates: χ (eastward), ϕ (northward), and σ (vertical), with $\sigma = (z-\zeta)/(h+\zeta)$, where z is the Cartesian vertical coordinate, h is the water depth relative to the reference sea level ($z = 0$), and ζ is the elevation above this; the total water depth is $H = h + \zeta$. While σ is the vertical coordinate, it is discretized onto levels which vary in the horizontal in σ space; this is described in section 3.1.

2.1. Equation of State

The density is defined by an approximation to the full UNESCO equation of state: $\rho(T,S,p) = \rho(T,S,0)+\rho'(T,S,p)$, where T is the potential temperature (°C), S is the salinity (practical salinity units (psu)), and p is the pressure relative to the sea surface. Here $\rho(T,S,0)$ is taken from the UNESCO equation of state and

$$\rho'(T,S,p) = 10^4 \frac{p}{c^2}\left(1 - 0.20\frac{p}{c^2}\right), \tag{1}$$

with

$$\begin{aligned} c &= 1449.2 + 1.34(S-35) + 4.55T - 0.045T^2 \\ &\quad +0.00821p + 15.0\times 10^{-9}p^2, \end{aligned} \tag{2}$$

following *Mellor* [1991].

For accuracy in the numerical calculation we define the buoyancy $b = b_0 + b'$, where the "potential" buoyancy is $b_0 = g[\rho_0 - \rho(T,S,0)]/\rho_0$ ($\rho_0 = 1027$ kg m^{-3} is the reference density) and the variation of compressibility with temperature and salinity is accounted for by $b' = g[\overline{\rho'(Z)} - \overline{\rho']}/\rho_0$, with $Z = z - \zeta = \sigma H$. Our initial condition gives $\overline{\rho'(Z)} = -0.004564Z$. The total (hydrostatic) pressure is then given by

$$P = P_a + \rho_0(\psi + g\zeta - gz) + 0.002282gZ^2, \tag{3}$$

where P_a is the atmospheric pressure and $\psi = H\int_0^\sigma b d\sigma$.

2.2. Equations of Motion

We solve the incompressible, hydrostatic, Boussinesq equations of motion, and to allow time splitting between barotropic and baroclinic components, these equations are divided into depth varying and depth independent parts; so the eastward velocity is $u = \overline{u}(\chi,\phi,t) + u_r(\chi,\phi,\sigma,t)$ and the northward velocity is $v = \overline{v} + v_r$. The depth mean equations are

$$\begin{aligned} \frac{\partial \overline{u}}{\partial t} &= f\overline{v} - (R\cos\phi)^{-1}\left[g\frac{\partial \zeta}{\partial \chi} + \rho_0^{-1}\frac{\partial P_a}{\partial \chi}\right] \\ &\quad +H^{-1}[F_S - F_B] + NLB_\chi, \end{aligned} \tag{4}$$

and

$$\begin{aligned} \frac{\partial \overline{v}}{\partial t} &= -f\overline{u} - R^{-1}\left[g\frac{\partial \zeta}{\partial \phi} + \rho_0^{-1}\frac{\partial P_a}{\partial \phi}\right] \\ &\quad +H^{-1}[G_S - G_B] + NLB_\phi, \end{aligned} \tag{5}$$

while the equations for the depth varying components are

$$\frac{\partial u_r}{\partial t} = -L(u) + fv_r + \frac{uv\tan\phi}{R} - \Pi_\chi + D(u) - H^{-1}[F_S - F_B] - NLB_\chi, \quad (6)$$

and

$$\frac{\partial v_r}{\partial t} = -L(v) - fu_r - \frac{u^2\tan\phi}{R} - \Pi_\phi + D(v) - H^{-1}[G_S - G_B] - NLB_\phi, \quad (7)$$

where R is the radius of the earth and the buoyancy terms are given by

$$\Pi_\chi = (R\cos\phi)^{-1}\left.\frac{\partial\psi}{\partial\chi}\right|_z \qquad \Pi_\phi = R^{-1}\left.\frac{\partial\psi}{\partial\phi}\right|_z. \quad (8)$$

These have not been transformed onto σ coordinates (unlike in previous applications) because of the particular method of solution used here (section 3.4). The depth means of the nonlinear and buoyancy terms are

$$NLB_\chi = \int_{-1}^{0}\left[-L(u) + \frac{uv\tan\phi}{R} - \Pi_\chi\right]d\sigma, \quad (9)$$

$$NLB_\phi = \int_{-1}^{0}\left[-L(v) + \frac{u^2\tan\phi}{R} - \Pi_\phi\right]d\sigma. \quad (10)$$

The advection terms are given by

$$L(a) = \frac{u}{R\cos\phi}\frac{\partial a}{\partial\chi} + \frac{v}{R}\frac{\partial a}{\partial\phi} + \Omega\frac{\partial a}{\partial\sigma}, \quad (11)$$

with

$$\Omega = -\frac{\sigma}{H}\frac{\partial\zeta}{\partial t} - (HR\cos\phi)^{-1}\times \left[\frac{\partial}{\partial\chi}\left(H\int_0^\sigma u d\sigma\right) + \frac{\partial}{\partial\phi}\left(H\cos\phi\int_0^\sigma v d\sigma\right)\right]. \quad (12)$$

As is common practice in models of this type, the vertical gradients of the stresses, $(\tau_{z\chi}, \tau_{z\phi})/\rho$, have been replaced by a diffusion term:

$$D(a) = H^{-2}\frac{\partial}{\partial\sigma}\left(K_z\frac{\partial a}{\partial\sigma}\right), \quad (13)$$

where K_z is the eddy viscosity defined in section 2.3. The equation for the free surface is

$$\frac{\partial\zeta}{\partial t} = -(R\cos\phi)^{-1}\left[\frac{\partial}{\partial\chi}(H\overline{u}) + \frac{\partial}{\partial\phi}(H\cos\phi\overline{v})\right]. \quad (14)$$

We use slip vertical boundary conditions: the components of surface and bottom stress and the corresponding friction coefficients are given by

$$(F_s, G_s) = c_s\frac{\rho_A}{\rho_0}(u_w, v_w)\sqrt{u_w^2 + v_w^2}, \qquad c_s = 0.63 + 0.66\sqrt{u_w^2 + v_w^2}, \quad (15)$$

following *Smith and Banke* [1975], where (u_w, v_w) is the wind velocity at 10 m and

$$(F_B, G_B) = c_B(u_B, v_B)\sqrt{u_B^2 + v_B^2}, \qquad c_B = \left[\kappa^{-1}log\left(\frac{\delta}{z_0}\right)\right]^{-2}, \quad c_B > 0.005, \quad (16)$$

following *Blumberg and Mellor* [1987]. The near bed velocity (u_B, v_B) is defined at a depth δ above the sea bed, the roughness length is taken to be $z_0 = 0.003$ m and $\kappa = 0.41$ is von Karman's constant. The transport equation for temperature T (and salinity S) is

$$\frac{\partial T}{\partial t} = -L(T) + D(T), \quad (17)$$

which uses the eddy diffusivity K_H (defined in section 2.3).

2.3. Turbulence Closure

To estimate the vertical eddy viscosity and diffusivity we use the Mellor-Yamada-Galperin level 2.5 turbulence closure scheme [*Mellor and Yamada*, 1974; *Galperin et al.*, 1988], with an algebraic mixing length. This results in a one equation, second moment closure lying somewhere between level 2 (steady state) and level 2.5 (two equation). We have included in this scheme a number of modifications which, while not necessarily optimal, were found to improve the on-shelf comparison between model and observations (both CTD and advanced very high resolution radiometer (AVHRR)), in this particular application.

The evolution of q^2 (twice the turbulent kinetic energy density) is given by

$$\frac{\partial q^2}{\partial t} = 2K_z M^2 - 2(K_H - \alpha K_z)N^2 - \frac{2q^3}{B_1 l} + D(q^2), \quad (18)$$

where

$$M^2 = H^{-2}\left[\left(\frac{\partial u}{\partial\sigma}\right)^2 + \left(\frac{\partial v}{\partial\sigma}\right)^2\right], \qquad N^2 = H^{-1}\frac{\partial b_0}{\partial\sigma}, \quad (19)$$

and $B_1 = 16.6$. The term in αK_z (with $\alpha = 0.7$) is a simple representation of vertical mixing by long wavelength internal waves following *Mellor* [1989].

There are many choices of algebraic mixing length, l, [see, e.g., *Xing and Davis*, 1996], and we have not evaluated all these options but instead use the Bakhmetev scale since *Holt and James* [1999b] show this gives reasonable results in the North Sea. We modify the length scale in deep water so that $l = \kappa H l_0(\sigma)$, where $h \le h_c$,

$$l_0 = (1+\sigma)(-\sigma)^{0.5}, \quad (20)$$

and where $h > h_c$

$$l_0 = \begin{cases} \frac{h_c}{h}\left(1 + \sigma\frac{h}{h_c}\right)\left(-\sigma\frac{h}{h_c}\right)^{0.5} & \sigma \ge \frac{-h_c}{3h} \\ \frac{2\sqrt{3}}{9}\frac{h_c}{h} & \frac{-h_c}{3h} > \sigma > \frac{2h_c}{3h} - 1 \\ (1+\sigma)\left(1 - \frac{h}{h_c}(1+\sigma)\right)^{0.5} & \sigma \le \frac{2h_c}{3h} - 1. \end{cases} \quad (21)$$

This maintains the surface and near-bed mixing length profiles at a water depth of h_c, (=150 m for this work) into deeper water, with intermediate depths in the water column taking the maximum value at $h = h_c$. Defining the profile in this way simulates, in an arbitrary fashion, the eddy scale becoming independent of water depth in deep water and prevents l increasing without limit with h. The eddy size in stratified water is limited according to the Ozmidov length scale (for dissipation ϵ), $L = (\epsilon/N^3)^{1/2}$. Hence we impose a limit on l proportional to this, following *Galperin et al.* [1988]:

$$l^2 < 0.28\frac{q^2}{N^2}. \tag{22}$$

The near-bed boundary condition arises from a steady state balance between shear and dissipation:

$$q^2|_{\sigma=-1} = B_1^{2/3}\sqrt{(F_B^2 + G_B^2)}, \tag{23}$$

whereas at the surface a balance between diffusion and dissipation is used to represent the flux of turbulence from surface wave breaking. Following *Craig and Banner* [1994, equation (24)] this gives

$$q^2|_{\sigma=0} = \alpha_{\text{wave}}^{2/3}(3B_1/S_q)^{1/3}\sqrt{(F_S^2 + G_S^2)}, \tag{24}$$

with $\alpha_{\text{wave}} = 100$. For a given stress, this leads to an increase in the value of the surface turbulence by a factor of ~ 20 above the sea bed boundary condition. This crude representation of surface wave effects leads to an improvement in the summer thermocline depth but is flawed in a number of respects. First, no spatial and temporal variation of the wave energy factor, α_{wave}, is included, and second the vertical resolution is unable to resolve the narrow region in which this surface turbulence is dissipated, so the effects are allowed to penetrate deeper than the work of *Craig and Banner* [1994] would suggest.

This system is closed by

$$K_z = S_M l q \quad K_H = S_H l q \quad K_q = S_q l q, \tag{25}$$

using the stability relations from *Galperin et al.* [1988]:

$$\begin{aligned} S_M &= \frac{0.3933 - 3.086G}{(1 - 34.68G)(1 - 6.127G)}, \\ S_H &= \frac{0.4939}{1.0 - 34.68G}, \quad S_q = 0.2, \end{aligned} \tag{26}$$

where $G = -l^2N^2/q^2$ and (22) gives $G > -0.28$. K_q is the coefficient for the vertical diffusion of q^2. In unstably stratified conditions, a convective adjustment scheme is used to mix vertically before the diffusivities are calculated; this is described in section 3.

3. Model Description: Numerical Solution

3.1. Grid

The region shown in Figure 1, ranging from 48° to 63°N and from 12°W to 13°E is divided into a 1/9° latitude by 1/6° longitude grid with $(i, j) = (1, 1)$ being at the southwest corner and $i = 1..150$, $j = 1..134$. The variables are arranged on an *Arakawa* [1972] B grid, so both components of velocity are defined (u points) half a grid spacing to the southwest of the points where scalar variables are defined (b points). The most southwestern scalar point is at (11 5/6°W, 48 1/9°N). The open and land boundaries of the model lie along b points to remove the need for a horizontal velocity boundary condition at the land boundaries.

The water column at each grid point is divided into N (=20 for this work) σ levels, and Figure 2 shows a schematic of the levels at a grid point. These are indexed $k = 0..N-1$, with levels $k = 0$ and $k = N - 1$ lying below the sea bed and above the sea surface, respectively, to facilitate the use of flux boundary conditions, hence levels $k = 1..N - 2$ are interior to the model. To maintain resolution near the surface in deep water, we allow the spacing of the σ levels to vary in the horizontal, according to the transformation

$$\begin{aligned} \sigma_{k-0.5} &= S_k + \tfrac{h_{i,j}-h_c}{h_{i,j}}[C(S_k) - S_k] \quad h_{i,j} > h_c \\ &= S_k \qquad\qquad\qquad\qquad\quad h_{i,j} \le h_c, \end{aligned} \tag{27}$$

where S_k are $N - 1$ evenly spaced levels between $\sigma = -1$ and $\sigma = 0$. Gradient variables are defined on these levels and state variables on $\sigma_k = (\sigma_{k-0.5} + \sigma_{k+0.5})/2$. The deviation from the usual σ levels is given by

$$\begin{aligned} C(S_k) &= (1 - B)\frac{\sinh(\theta S_k)}{\sinh(\theta)} \\ &+ B\frac{\tanh[\theta(S_k + 0.5)] - \tanh(0.5\theta)}{2\tanh(0.5\theta)}. \end{aligned} \tag{28}$$

This follows the s coordinate transformation of *Song and Haidvogel* [1994], except here we retain the definition of σ, so the spacing of the levels in σ space does not vary with time. For the present work we use the parameters $h_c = 150$ m, $\theta = 5$, and $B = 0.25$ to give an increased resolution only at the surface. For example, Figure 3 shows the model levels for an east-west section at 55.111°N; at a depth of 1800 m there are seven levels shallower than 200 m, in contrast to only two when evenly spaced σ coordinates are used. The equations of motion (equations (6) and (7)) require no further transformation when these levels are used since the advection scheme employed (section 3.3) is a finite volume formulation and the pressure gradients are calculated by interpolating the pressure onto horizontal planes (section 3.4).

3.2. The Depth Mean Solutions

The equations for the surface elevation (equation 14) and depth mean currents (equations (4) and (5)) are integrated forward in time (using centred space forward time differencing) with a time step of $\Delta t/10$, where $\Delta t = 400$ s is the (long) baroclinic time step. The surface elevations are filtered using the method described by *Killworth et al.* [1991] to prevent the "checkerboard" pattern of grid-scale noise which is sometimes found when using the B grid.

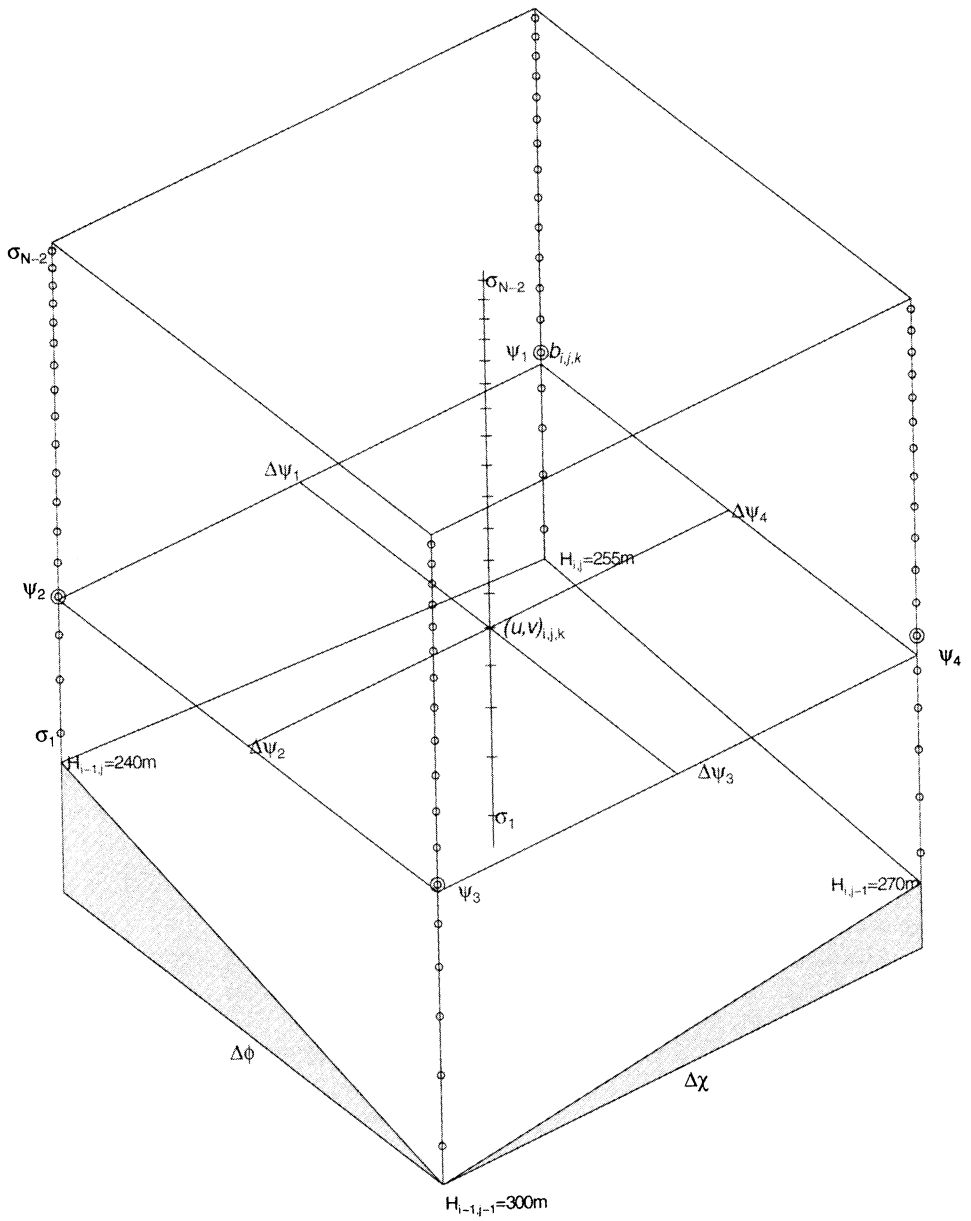

Figure 2. The arrangement of points on the B grid. Open circles and crosses are the σ levels at the b points and u points, respectively. The vertical spacing is dictated by the s coordinate transform described in section 3.1. Also shown is the horizontal plane, at $k = 5$ in this example, used to calculate the pressure gradients. The pressures at the corners of this plane are estimated on the sigma levels down to the double circles and from a linear interpolation of the buoyancy between these and the plane.

3.3. Advection

In order to maintain horizontal gradients and minimize numerical diffusion the advection of momentum and scalars uses the PPM scheme [*Colella and Woodward*, 1984; *James*, 1996]. This assumes the variables vary parabolically across the grid boxes, with the mean in the grid box, $\overline{a}$, taken to be the value at the grid point, $a_{i,j,k}$. The parabolas are then defined by

$$\begin{aligned} a(\eta) &= a_L + \eta[a_R - a_L + a_6(1-\eta)], \\ a_6 &= 6\overline{a} - 3(a_L + a_R), \end{aligned} \tag{29}$$

where the coordinate η varies from 0 to 1 across the grid box. The left and right values, a_L and a_R, are found initially by interpolating a quartic polynomial fit to the integral of a. These are adjusted so that no new extrema are introduced by the parabolas. The advective flux is then calculated by integrating the parabolas in an upwind sense. After horizontal advection, the PPM scheme is used in the vertical to adjust the σ levels back to their original spacing; this determines the flux across the vertical faces of the grid boxes. For scalar variables the depth mean flux used in the advection step is the sum of the fluxes calculated during each of the barotropic

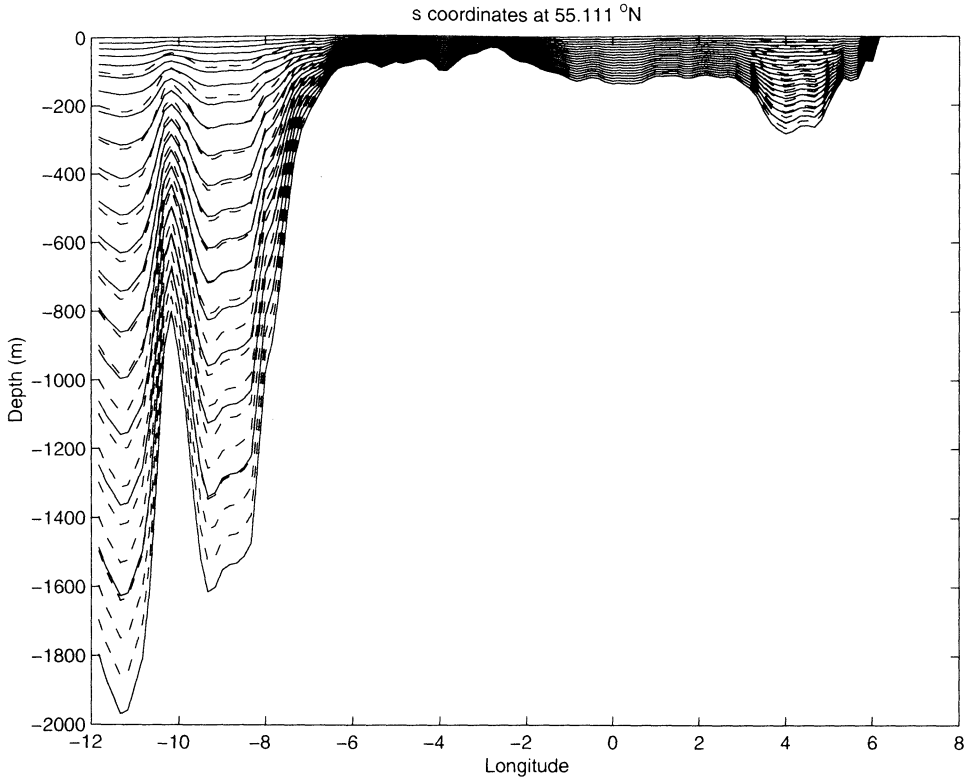

Figure 3. The model coordinate surfaces at 55.111°N after the s coordinate transform (solid); and the untransformed σ levels (dashed).

time steps (including the equivalent flux for the Killworth filter). This ensures that the depth at the end of the advection step is identical to that at the end of the barotropic step, so scalars are conserved during advection.

3.4. Horizontal Pressure Gradients

A novel method of estimating the horizontal pressure gradient term is used here since the model domain includes regions of extremely steep topography (with depth changes of up to 838 m between grid points). The traditional method of calculating the horizontal pressure gradient in σ coordinate models is to estimate the pressure (or density) gradients along σ levels and then correct these for the slope of the coordinates. The source of error in this is well documented [*Haney*, 1991; *Mellor et al.*, 1994]: in the case of a flat thermocline overlying steep topography, both these terms are of the same magnitude and should cancel to zero; however, this generally leads to a significant truncation error, which can drive erroneous currents. A number of methods of overcoming this problem have been suggested and successfully applied [e.g. *Stelling and van Kester*, 1994; *Slørdal*, 1997]. The approach adopted here involves estimating the four pressure gradients at the edges of the horizontal plane (an example is shown in Figure 2) with $(u,v)_{i,j,k}$ defined at the center and the corners being at the b columns (i,j),$(i-1,j)$, $(i-1,j-1)$, and $(i,j-1)$; for simplicity these are labeled $q = 1..4$, and the vertical index for the u point is dropped. The depth of the plane is

$$z = \frac{1}{4}(\sigma \sum_q H_q + \sum_q \zeta_q) \tag{30}$$

and at b column, q, this is at $\sigma_q = (z-\zeta_q)/H_q$. The nearest σ levels, k_q, above the plane (shown as double circles in Figure 2) lie at a fractional distance, $r = (\sigma_{k_q} - \sigma_q)/(\sigma_{k_q} - \sigma_{k_q-1})$, from the plane. If the buoyancy is taken to vary linearly between σ levels, the pressure due to this interval can be estimated, and the pressure at σ_q can then be written as

$$\begin{aligned}\psi_q = \; & -0.5\delta\sigma[b_{q,N-2} + \sum_{k=k_q}^{N-2}(b_{q,k} + b_{q,k+1}) \\ & +(2r - r^2)b_{q,k_q} + r^2 b_{q,k_q-1}],\end{aligned} \tag{31}$$

for $1 \le k_q \le N-2$, and

$$\psi_q = -0.5\delta\sigma[(2r - r^2)b_{q,k_q} + r^2 b_{q,k_q-1}], \tag{32}$$

for $k_q = N-1$; in this calculation, level $k = N-1$ is at the sea surface, where the buoyancy is defined by $b_{q,N-1} = b_{0q,N-2}$.

The pressure gradients along the edges of the plane are then

$$\begin{aligned}\Delta\psi_1 &= \psi_1 - \psi_2, \quad \Delta\psi_2 = \psi_2 - \psi_3, \\ \Delta\psi_3 &= \psi_4 - \psi_3, \quad \Delta\psi_4 = \psi_1 - \psi_4,\end{aligned} \tag{33}$$

and the corresponding changes in velocity are

$$\Delta u_{i,j,k} = -0.5\frac{\Delta t}{R\cos\phi\Delta\chi}(\Delta\psi_1 + \Delta\psi_3),$$

$$\Delta v_{i,j,k} = -0.5\frac{\Delta t}{R\Delta\phi}(\Delta\psi_2 + \Delta\psi_4). \quad (34)$$

This technique allows a straight forward treatment of cases where the sea bed lies above the plane at one or more of the surrounding b points; if either of the corners on an edge are below the sea bed, then the corresponding pressure gradient takes the last defined value above it. This assumes the isopycnals are horizontal close to the sea bed and does not reflect the correct boundary condition for temperature and salinity (zero normal gradients). However, the diffusive layers in which the thermoclines and haloclines curve to meet this condition are not well resolved in this model.

This method has been tested against the pressure gradient given by an analytically defined thermocline and gives significantly more accurate results than the conventional method when the thermocline is flat or sloping in the opposite sense to the σ levels. Both methods give equally good results when the thermocline slopes in the same sense as the σ levels.

3.5. Vertical Mixing

The vertical diffusion of scalars and momentum uses a fully implicit numerical scheme, and in the case of momentum, the surface and bottom stresses are introduced as fluxes at this stage. The diffusivities used in these calculations are estimated from (25), with l limited by stratification (equation (22)). The equation for q^2 (equation (18)) is integrated forward in time with the shear, buoyancy, and dissipation terms being split into implicit and explicit parts by a Taylor expansion about the current time level (following *Annan* [1999]). The diffusion term is solved implicitly with values of K_q estimated between the values of q^2 by arithmetic averaging.

3.6. Convective Adjustment

As suggested by *Deleersnijder and Luyten* [1994], we find that the turbulence closure described in section 2.3 provides an inadequate treatment of statically unstable layers. This is not unexpected since convection is not a subgrid scale process so is not well represented by diffusion at a grid point. Moreover, tiny values of $N^2 < 0$ are found to give very large diffusivities, and under surface cooling conditions, these propagate down the water column but take a number of time steps to mix the surface layer.

Instead of the turbulence closure scheme, we use a simple convective adjustment procedure to more effectively mix unstable density gradients. At each horizontal grid point, the model searches down in the vertical for a point where $N^2_{k-0.5} < 0$, at σ level $k = k'$. The temperature and salinity at k' is then repeatedly averaged with Δk points below until the resulting buoyancy $b_0(\overline{T}, \overline{S})_{k'-\Delta k} > b_0(T, S)_{k'-\Delta k-1}$ (here an overbar indicates an average from k' to $k' - \Delta k$). The temperature and salinity in this interval is then replaced by $\overline{T}$ and $\overline{S}$. If necessary, this procedure is repeated for points above k'. The velocity field is also adjusted by convection; prior to the adjustment at b points, the T and S values are interpolated onto the u points and (u, v) are averaged in the vertical according to the above scheme.

Because of its arbitrary nature, the use of this convective adjustment scheme is less than satisfactory. This is particularly the case for velocities; while its effects on their profiles are not great, it may result in excessive mixing under unstratified conditions. However, we do find the use of this adjustment somewhat improves the comparison with SST observations, but a more satisfactory method of treating statically unstable conditions needs to be sought.

3.7. Initial and Boundary Conditions

The model is initialized from rest on November 1 1988 with a three-dimensional climatology of temperature and salinity [R. Proctor, POL, personal communication, 1990] and run forward for 1 year. The period November 1988 to October 1989 is chosen both because of the availability of atmospheric forcing data and to allow a comparison with the North Sea Project (NSP) observations [*Charnock et al.*, 1994] and with model results from *Holt and James* [1999b]. The elevations use a flux/radiation boundary condition, with the external elevation and depth mean velocity determined from 15 tidal constituents taken from a tidal model of the northeast Atlantic [*Flather*, 1981]. We do not include a surge or density component of the boundary currents and elevations because sufficient information to specify these is not available at the present time. Similarly, the effect of large-scale atmospheric pressure gradients (the "inverse barometer effect") are not included in the boundary conditions. The implications of omitting these boundary components are discussed in HJJ.

Temperature and salinity are relaxed to climatological values in a region of four grid points from the model boundaries. These values, $T0$, are taken to be the linear interpolation in time between the monthly three-dimensional climatologies (such as those used in the initial condition), which are assumed to be representative of the value on the 15th of the month. We find these temperature and salinity fields contain some small-scale variations, for example, on the continental slope, which we remove by smoothing on horizontal planes since these variations cannot adjust and may drive erroneous currents. The effects of this smoothing are examined in HJJ. The temperature at the grid points $p = 0 \ldots 3$ from the western boundary are given by

$$T_{i+p,j} = rT0_{i+p,j} + (1-r)T_{i+p,j}, \quad r = (4-p)/4, \quad (35)$$

with similar equations for the northern and southern boundaries and for salinity. The corresponding relaxation timescale is $t \sim \Delta t/r$; ~ 26 min for $p = 3$.

The sea surface is forced by three hourly data from the U.K. Meteorological Office weather prediction model, and the temperature is updated by the heat fluxes calculated from bulk formulae using this data (following *Gill* [1982]) and downwelling solar radiation (with a decay scale taken to be $0.154\ \mathrm{m}^{-1}$). Details of these are given by *Holt and James* [1999b] and will not be repeated here. At present, there is no surface salinity flux in this model; however, freshwater inputs are determined from daily discharge data from 36 U.K. and continental rivers (data from the U.K. Environment

Agency), and the exchange with the Baltic and the Kattegat is incorporated using salinity and volume flow data from the Danish Hydrographic Institute DYNOCS experiment.

4. Sea Surface Temperature and Salinity Structure

4.1. Temperature

To assess the model's sea surface temperature structure, we use 9 km AVHRR satellite data for the period of the model run (from the NOAA/NASA Ocean Pathfinder satellite, downloaded from http://podaac.jpl.nasa.gov/sst). These data are accurate to about ~ 0.5°C in this region [*Annan and Hargreaves*, 1999]. Mean and rms deviations are generated from the twice daily AVHRR images by interpolating the available measurements onto the model grid and using only the corresponding model values, so both model and observations are similarly biased to "cloud free" values. For example, in March, there are, on average, 14 available measurements at each model grid point (out of a possible maximum of 62) and only 2% of the (noncoastal) model sea points have fewer than five values.

The composite mean SST for the model and AVHRR in January, March, and May 1989 are shown in Plate 1 and those of June, August and October 1989 are shown in Plate 2. Plate 1 demonstrates that the model is successful in reproducing the large-scale features of the observed SST structure under winter conditions. The large temperature difference between the Celtic Sea and the North Sea is well reproduced ($\sim$ 4°C in March decreasing to about $\sim$ 2°C in May). The model predicts the movement of this warmer water from the Celtic Sea up the shelf break and into the northern North Sea through the Fair Isle Channel and in a current east of the Shetland Isles (see HJJ). However, the model overpredicts the temperature of this water (and that in the deeper water to the northwest of the shelf edge) by $\sim$ 1°C. The presence of warmer shelf edge water is less pronounced in May and in the summer months (Plate 2); the large-scale temperature gradient is then primarily north-south in both model and observations, with the Celtic Sea and southern North Sea having similar temperatures. However, the model underpredicts this north-south gradient in the North Sea (for reasons which are discussed below).

The model has some success in reproducing the smaller-scale features seen in the observations; however, the composite satellite images generally show significantly more small-scale variability and patchiness than the model results. This is presumably due to subgrid scale phenomena (such as eddies and internal tides) which are present, but poorly re-

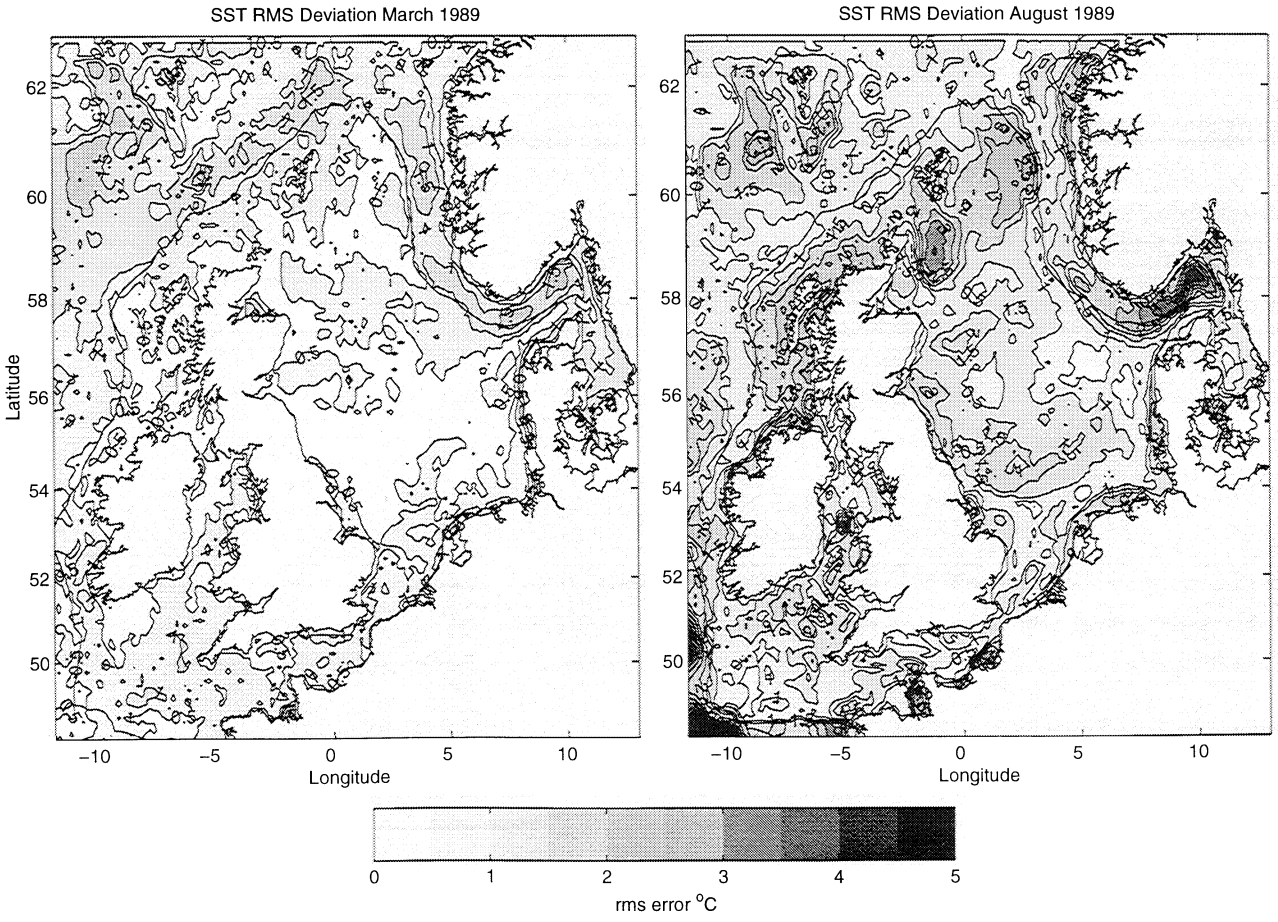

Figure 4. The rms deviation between modeled and observed SST. Statistics are derived from all available observations at each model grid point in March and August. The contour interval is 0.5°C.

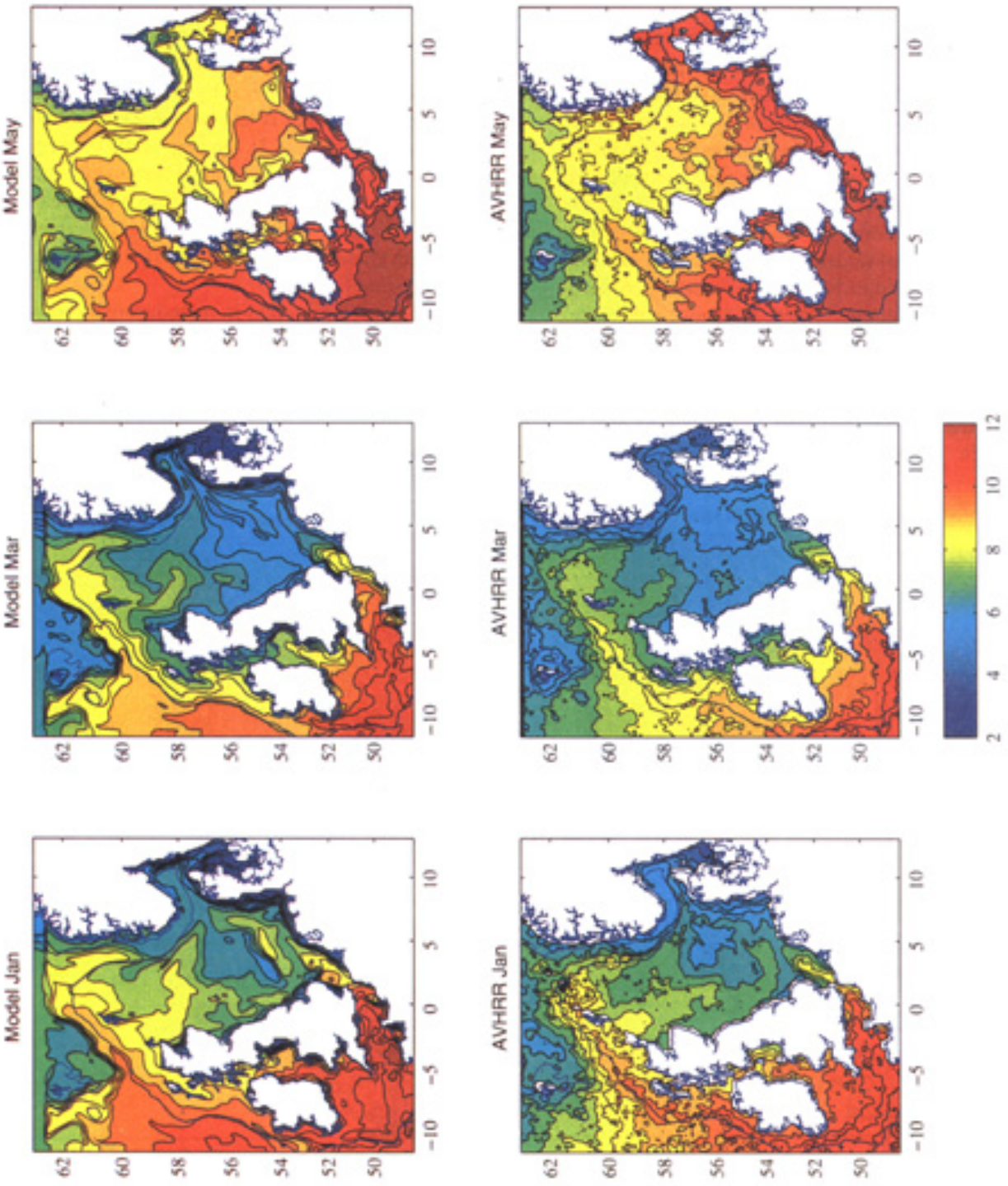

January, March, and May 1989. The contour interval is 0.5°C. Heavy lines show the 200 m contour in this and subsequent figures.

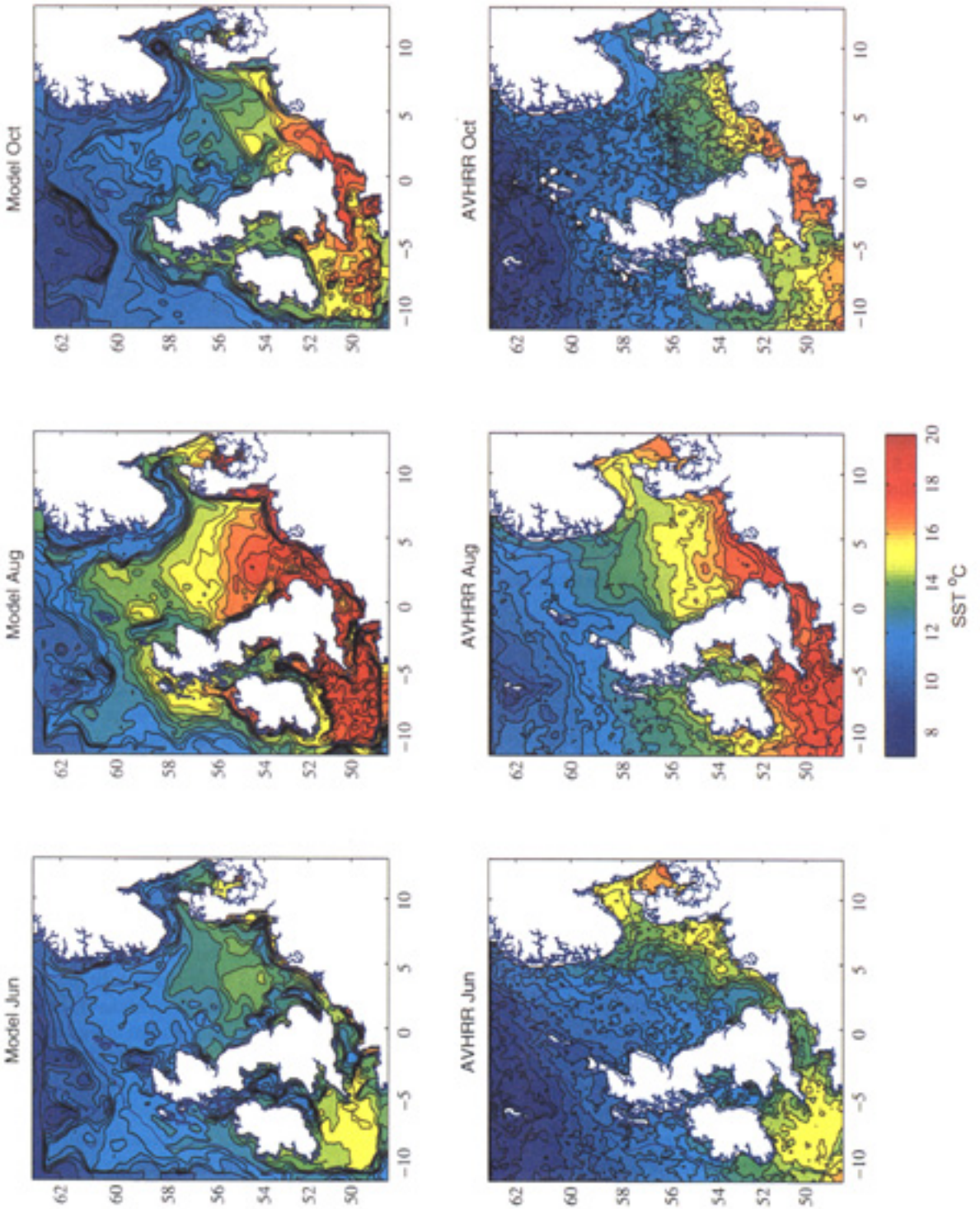

Plate 2. As Plate 1 for June, August, and October 1989.

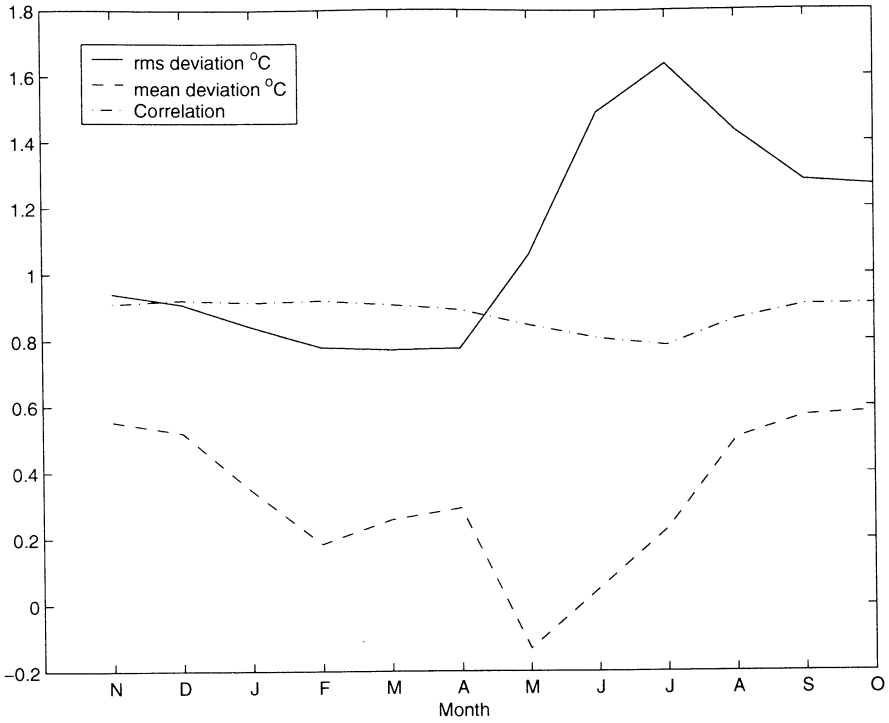

Figure 5. Monthly statistics comparing model and AVHRR SST calculated for the whole model domain (excluding the relaxation zones).

solved, in the observations but completely absent from the model simulations.

The warmer water ($\sim$ 8°C) entering the southern North Sea through the Dover Straits in January and March is well modeled and the temperature structure north of Ireland and west of Scotland is also accurately reproduced in these month. In January, the Irish Sea south of Anglesey has a similar temperature to the Celtic Sea in both model and observations. The Irish Sea cools down faster than the Celtic Sea, but an influx of warmer water through the St. George's channel (see HJJ) results in a tongue of $\sim$ 8°C water stretching from south to north Wales in March. The extent of this tongue is well modeled, and the waters in the central Irish Sea (around the Isle of Man) are between 7° and 7.5°C in both model and observations.

In June the thermal front between the Irish and Celtic Seas is apparent in both model and AVHRR, and throughout the summer the model shows a movement of water from the Irish Sea, around the south coast of Ireland. In August and October the observations do show a northward decrease in temperature near the southern Irish coast, which might indicate such a current; however, the gradients in these observations are much weaker than those in the model. Similarly, in August and October, evidence of a plume of cooler water down the east coast of the United Kingdom from the Firth of Forth to Holderness is present in both model and observations; but again the model produces a stronger horizontal temperature gradient than the observations.

The monthly rms deviations between model and AVHRR SST in March and August are shown in Figure 4: the sign of these errors can be inferred from Plates 1 and 2. The rms errors are less than 1°C over much of the model domain. Noticeable exceptions are in the Norwegian Trench, where the model overpredicts the winter temperatures and underpredicts the summer values, and the northwest corner of the model and along the section of the shelf edge west of Scotland where the model consistently overestimates the temperatures, presumably because of errors in the boundary forcing and the transport of warm water along the shelf break.

The underpredicted seasonal variation of the temperatures in the Norwegian Trench can be explained by the salinity stratification being too weak. This reduces the heating and cooling in the surface layer below that required by the observations. In model runs with evenly spaced σ coordinates, and hence poorer resolution in the trench, these errors are significantly increased (by $\sim$ 1°C in March). In the summer months the observations show little or no signal for the Norwegian coastal current (this is also apparent in the individual images) indicating a strongly isolated surface layer. This may well be due to the thermal stratification in the observations extending all the way to the surface or to the existence of a very thin surface layer, since the cloud-free days during which observations are available are likely to be those with the strongest heating and weakest winds. The model SST, however, is always at a distance $Z = 0.5\sigma_{N-2}H$ below the surface, so will only be comparable with the observations when these have a mixed layer of at least this depth. This supposition is supported by the temperature climatology (at $Z = -0.05H$), showing a distinct cold surface signal for the Norwegian Trench in the summer.

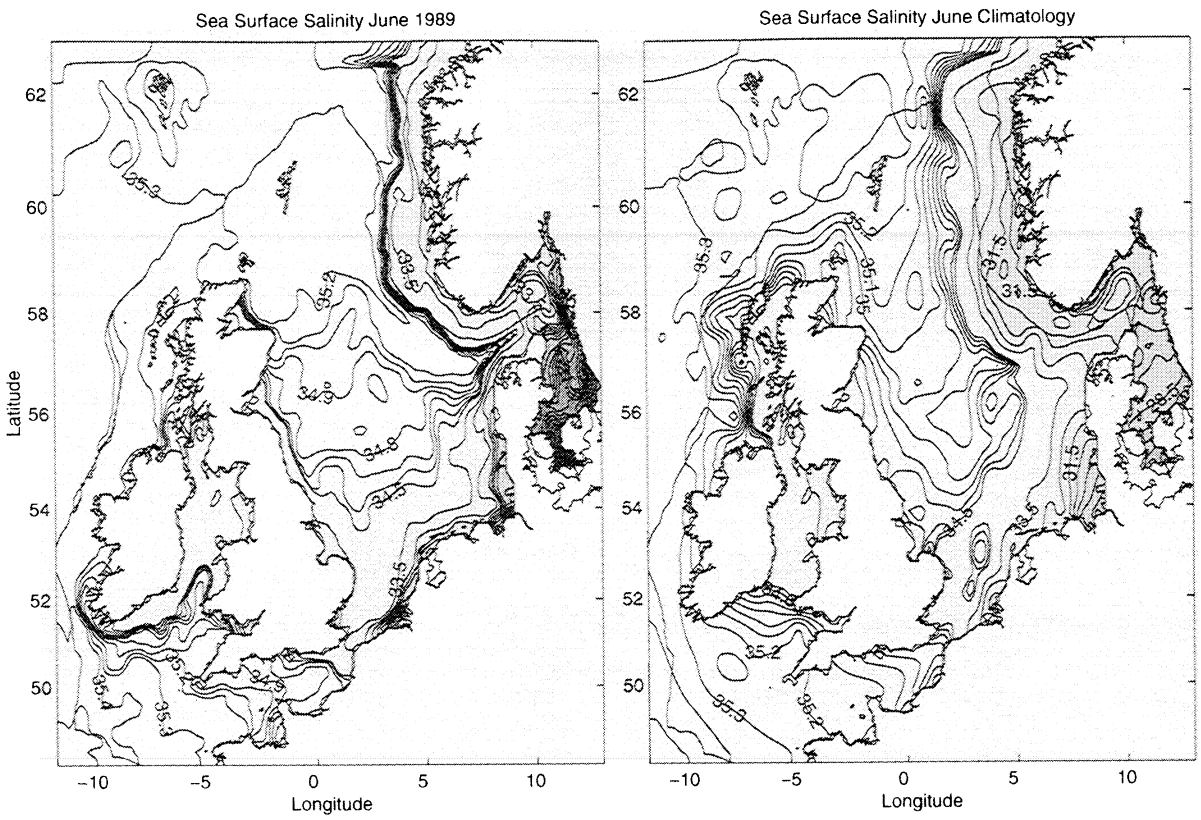

Figure 6. Sea surface salinity from the model and the climatology: average for June. The contour interval is 1 psu for $9.5 < S < 34.5$ psu.; and 0.1 psu for $S > 34.6$ psu.

The annual variation in mean and rms errors has been calculated using all the observations and corresponding model predictions (excluding the relaxation zones) in each month (Figure 5). These show the errors decrease through the winter months from their initial condition values in November. The rms error increases strongly between April and July, up to 1.6°C, but decreases in late summer, so the October value is only ~ 0.3°C greater than the previous November value. The overall mean errors are small (< 0.6°C) throughout the year and return to the initial condition value by October, suggesting there is no significant bias in the surface heat fluxes. The monthly spatial correlation between model and AVHRR varies between $r = 0.92$ in December and 0.78 in July, demonstrating the ability of the model to reproduce the overall spatial structure of the sea surface temperature.

4.2. Salinity

There is as yet no remotely sensed data available for salinity, so we compare the predicted sea surface salinity with climatological values; Figure 6 shows the results for June. The salinity fronts in the climatology would be expected to be much more diffuse than in reality because of the sparse nature of the data from which they where derived; indeed the model produces much sharper fronts. However, the general pattern is very similar in both model and climatology; the correlation is $r = 0.80$. The main regions of fresher water are the Irish Sea and the southern North Sea, owing to river outflows, and the Norwegian Trench, Skagerrak, and Kattegat owing to water from the Baltic. The strong surface current of fresher water from the Baltic into Kattegat and around the coast of Norway is the dominant salinity signal in this region. However, compared with the climatology the model tends to overestimate the salinity in the Norwegian Trench and underestimate it in the Kattegat. This may be due to the climatology not being representative of conditions in this year but is more likely owing to the resolution not being sufficient for the steep bathymetry in the Skagerrak; there is a strong and persistent circulation in the deep (600 m) water north of Denmark which appears to block the outflow from the Kattegat, hence limiting the extent and strength of the salinity stratification in the Norwegian Trench.

The freshwater signal of the Scottish coastal current is not well formed in the model. This signal arises from the northward flow through the North Channel of the Irish Sea, which we may well be underestimating (as discussed in HJJ), and from inputs from the Scottish coast, all of which are not included in our river data.

The sea surface salinity across the St. George's Channel and around the south coast of Ireland matches the structure seen in the model SST (Plate 2) indicating that cooler fresher water leaves the Irish Sea on the west side of the St. George's Channel, whereas warmer, more saline water enters on the east side.

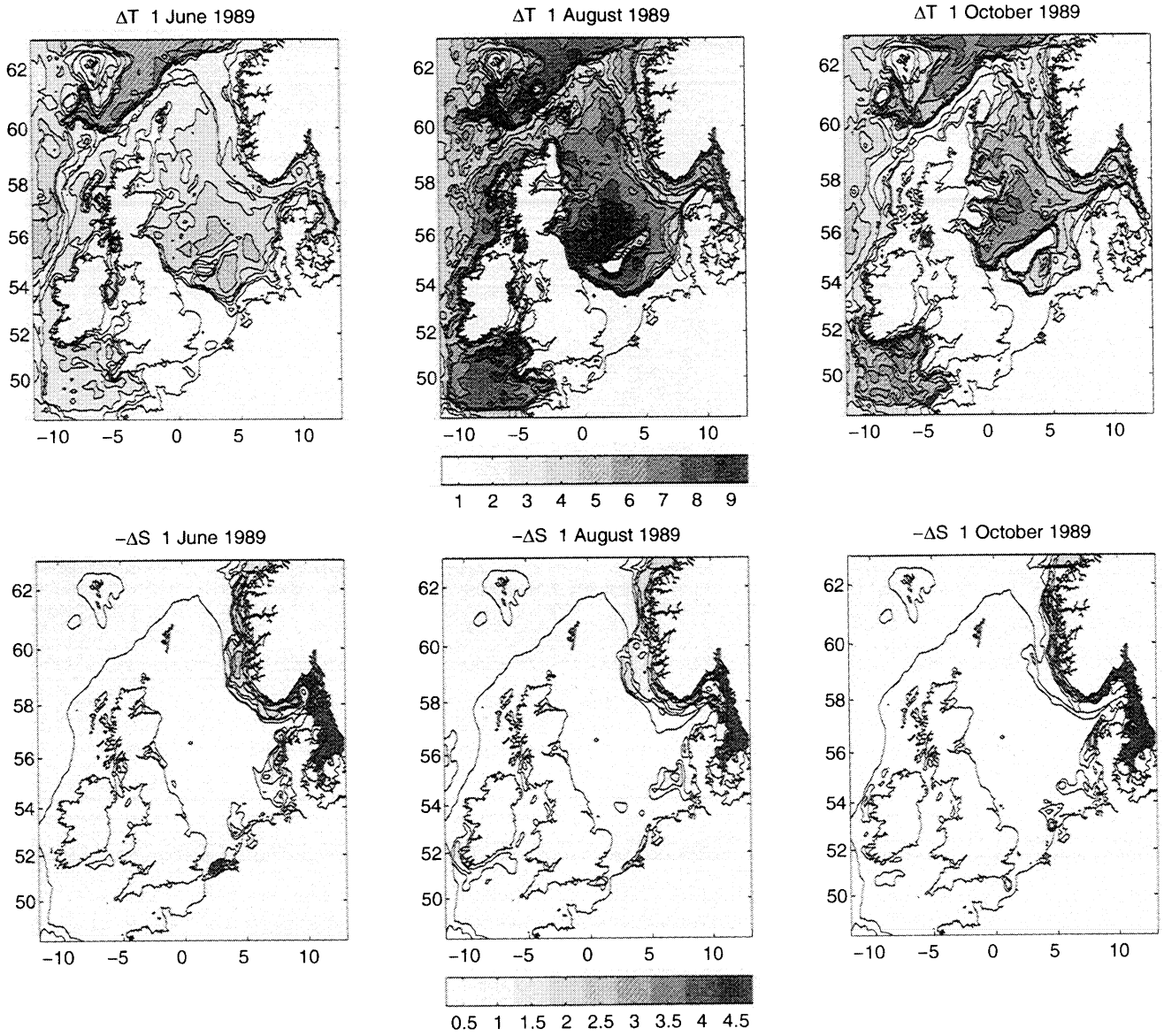

Figure 7. Daily mean surface to bed temperature difference and bed to surface salinity difference for June 1, August 1, and October 1, 1989. The contour intervals are 1°C and 0.5 psu.

5. Temperature and Salinity Stratification

The surface to bed temperature and salinity differences (ΔT and ΔS) on the 1st June, August, and October are shown in Figure 7. The on-shelf temperature stratification is well established at the beginning of June, intensifies through the summer, and is breaking down in October, especially in the Irish Sea and around the coast of Scotland. The main regions to remain unstratified throughout the summer are the English Channel, the Southern Bight of the North Sea, and the northeastern Irish sea.

The location of the thermal fronts in the Irish Sea are in good agreement with those observed by *Simpson and Hunter* [1974], stretching across the St. George's Channel and southwest from the Isle of Man to the Irish coast. The thermal front between the Irish and Celtic Seas primarily stretches across the St. George's Channel although the model does produce a narrow($\sim$1 grid spacing) band of stratification in the center of this channel as far as north Wales. The movement at the surface of cooler, fresher water, around the south coast of Ireland seen in Plate 2 and Figure 6 is not particularly evident in the temperature stratification before October 1.

The southern North Sea front extends further into the German Bight than in the 20 km resolution modeling study of *Holt and James* [1999b] and is more in accord with the frontal position estimated from the NSP measurements in that work and with the $\sim$ 2.5 km resolution model of *Proctor and James* [1996]. Figure 7 shows how the salinity stratification due to the outflow from the continental rivers aids the formation of thermal stratification close to the coast; this retreats away from the coast as the salinity stratification weak-

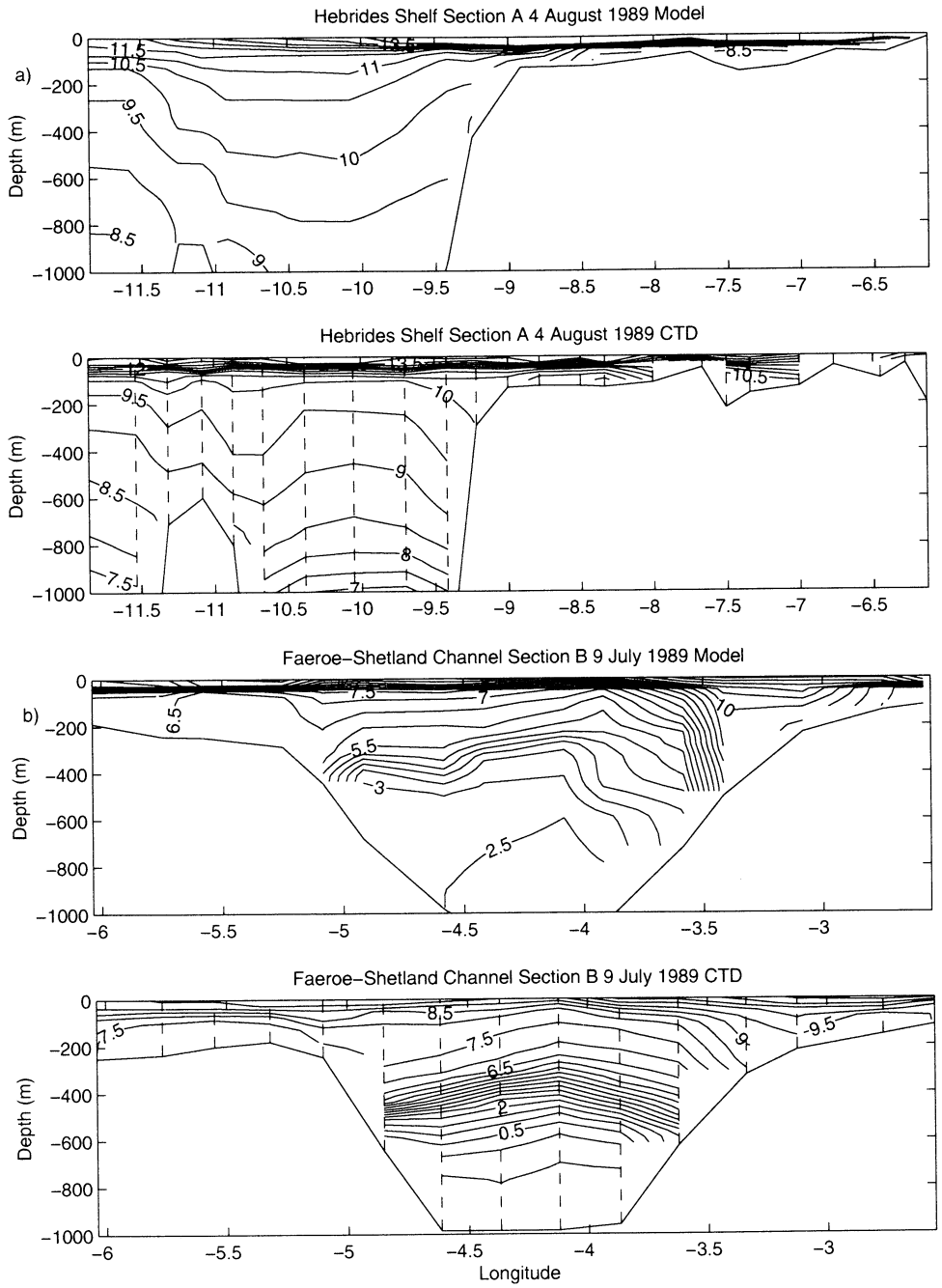

Figure 8. Model and CTD temperature and salinity sections. Dashed lines show the location of the CTD casts. (a) Temperature at section A across the Hebrides Shelf. The maximum water depth is 2275 m, but for clarity only the top 1000 m are shown. (b) Temperature at section B across the Faeroe-Shetland Channel. (c) $T$and S at section C across the central North Sea. (d) T and S at section D across the northern North Sea. The maximum water depth is 276 m, but for clarity only the top 200 m are shown. Model results in Figues 8a and 8b are only shown at the CTD locations; Figures 8c and 8d show the complete model field across the section. Contour intervals are 0.5°C and 0.1 psu.

ens in August and October. This is in agreement with the observations presented by *Holt and James* [1999b] which show stratification closer to the coast of Denmark in May than in August in this year.

The dominant salinity stratification is in the Norwegian coastal current, mirroring the dominant sea surface salinity signal seen in Figure 6. In August this stratification extends beyond the western side of the Norwegian Trench, possibly owing to eddy transport across the trench (HJJ shows the model produces baroclinic eddies in this region in August). By October 1, however, the region of salinity stratification has reduced to a narrow band around the coast of Norway.

Sections along the lines shown in Figure 1 are used to examine the model vertical structure in more detail and to com-

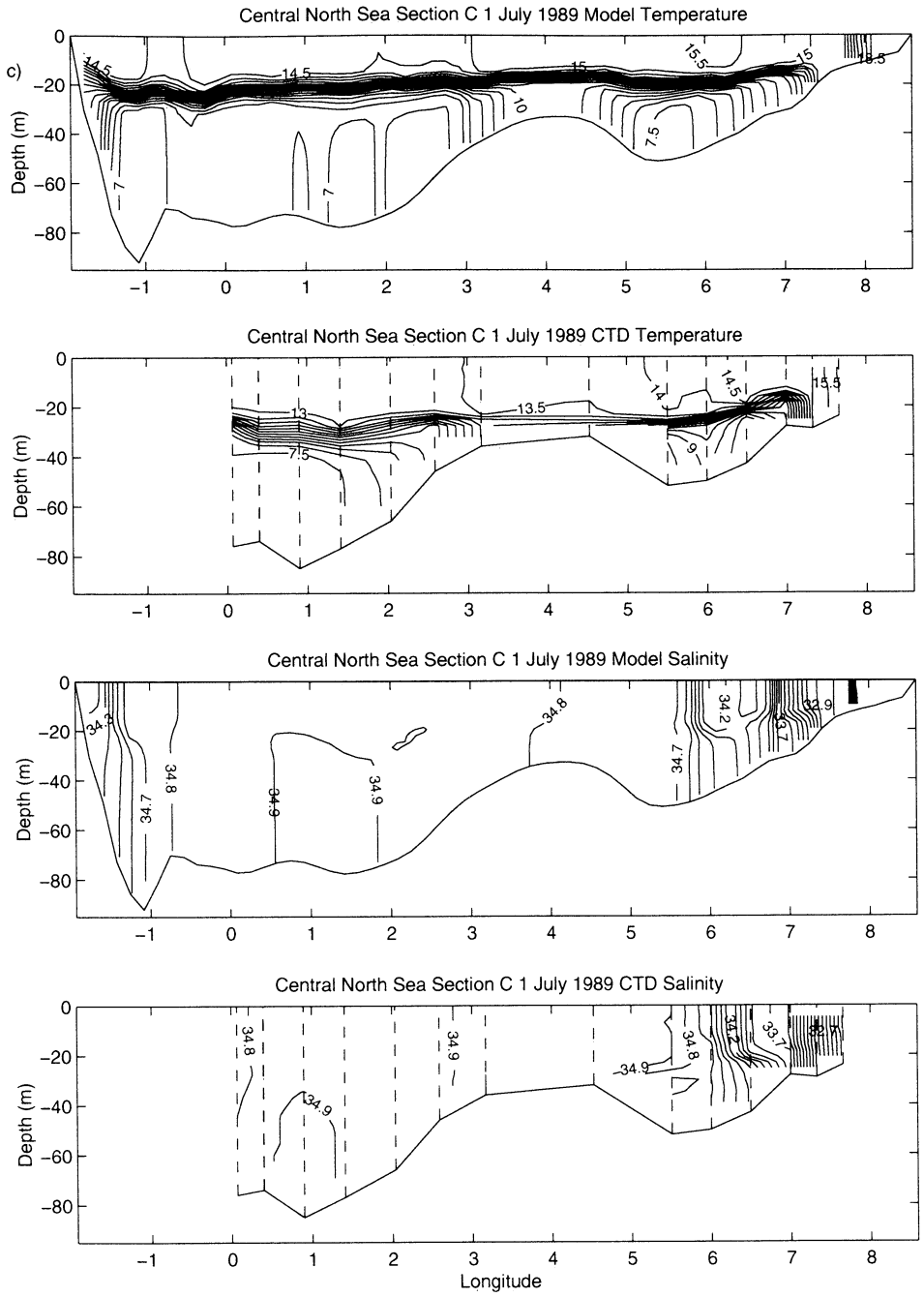

Figure 8. (continued)

pare this structure with CTD observations (Figures 8a-8d). Since the sections across the Hebrides shelf (Figure 8a) and across the Faeroe-Shetland Channel (Figure 8b) do not lie along model grid lines, the model sections are formed from data at the closest model grid point to the individual CTDs. Moreover, salinity is not shown for these sections since over the length of this run it is only determined by the evolution of the initial condition and by the boundary conditions. The CTD data is binned in the vertical onto the model levels and comparing these binned profiles with the original data suggests the resolution used here is adequate to reproduce the observed vertical temperature structure. There are a number of smaller-scale features in the CTD data that cannot be resolved with the present number of levels (and the chosen spacings); however, it is questionable whether the physics in the model, the forcing, and the horizontal resolution is adequate to reproduce these even at higher vertical resolution.

Figures 8a and 8b are primarily shown to demonstrate that the s coordinate transform permits a thermocline that crosses the shelf break with little variation with the topography. Figure 3 shows that such a thermocline would not be present at this resolution if evenly spaced σ levels had been used. Beyond this demonstration, however, the comparison is not particularly good. The thermoclines along

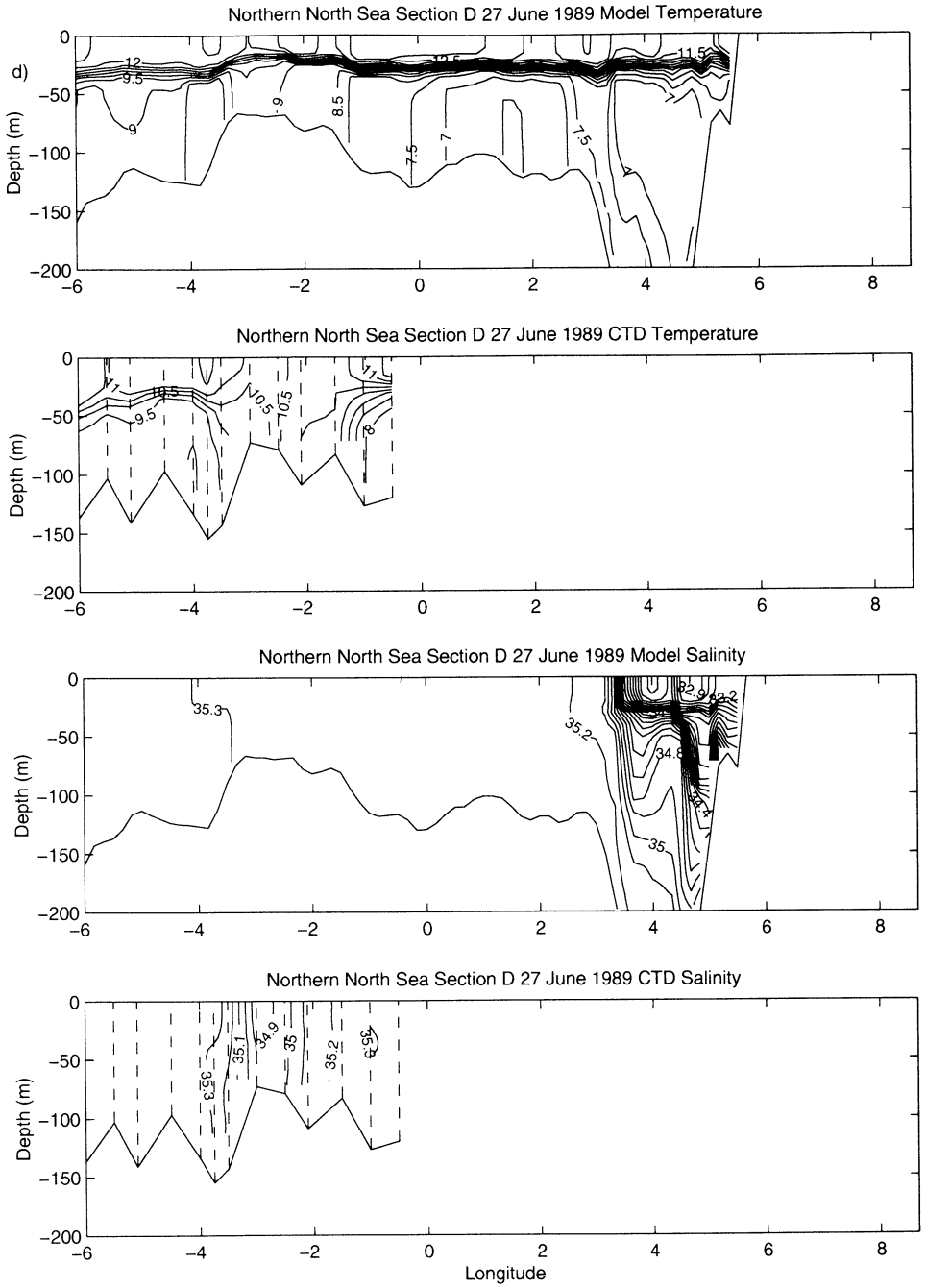

Figure 8. (continued)

these sections are too shallow, leading to the overestimation of summer SST in this region seen in Plate 2. Across both sections the model significantly overestimates the near-bed temperatures; these have not changed significantly from the initial condition, suggesting this is in error. Just south of the Hebrides shelf section (Figure 8a) there is a strong cyclonic eddy from $\sim$ 10°W to the model boundary with daily mean surface currents of up to 1.04 m s^{-1} (see HJJ). This strongly deepens the isotherms in comparison with the observations; from its spin-up on around July 15 to August 4 the 10°C isotherm at 10.4°W, 57.3°N deepens from 267 m to 491 m. In the Faeroe-Shetland Channel (Figure 8b) the midwater temperatures (down to $\sim$ 500 m) are in better agreement with observation, but below this the model overestimates the temperatures, suggesting it underestimates the southward transport of Norwegian Sea Deep Water through this channel; *Schlichtholz and Jankowski* [1993] show that there was a strong overflow ($0.65 \pm 0.56 \times 10^6$ m^3 s^{-1}) of this water mass in the summer of 1989.

The section across the central North Sea (Figure 8c) shows the model produces a better representation of the temperature and salinity structure in this region than at the deep water sections. The thermocline stretches the whole width of the CTD section, at an almost constant depth, ending in a

tidal mixing front at $\sim$ 7.25°E in both model and observations, as far as its position can be estimated from CTD casts at this spacing. Similarly, whether or not there are any fronts at this latitude on Dogger Bank cannot be determined from these observations. The thermocline predicted by the model is too sharp and too shallow across this region, suggesting the model is underpredicting diapycnal mixing and the wind deepening of the thermocline. This would account for the increased errors in the SST during the summer seen in Figures 4 and 5; the surface temperatures are overpredicted in Figure 8c, by $\sim$ 1.5°C, whereas the near-bed temperatures are underpredicted by $\sim$ 0.5°C to the west of Dogger bank and $\sim$ 1.5° to the east. The salinity signal at the eastern boundary of the North Sea is well modeled both in its horizontal extent (again estimation of this is limited by the CTD spacing) and the depth of the halocline. On the western side, CTD measurements were not made in the region of freshwater influence; however, the observations do show the 34.8 psu. contour is further east than in the model results, possibly suggesting that the river plumes on the east U.K. coast may not be wide enough in the model.

The section across the northern North Sea (Figure 8d) shows that the model is underestimating the thermocline depth and thickness and, as in the central North Sea, the surface temperatures are overestimated (by $\sim$ 1°C) and the near-bed temperatures underestimated (by $\sim$ 0.5°C). The observations show tidal mixing fronts on either side of the ridge between Orkney and Shetland. These are not apparent in the model on June 27 suggesting that this region stratifies too early; it is mixed on June 1 (Figure 7). The salinity measurements at this section show that while the model is in agreement with the observations on the west Shetland Shelf, there is a salinity minimum (of $\sim$ 34.9 psu.) in the Fair Isle Channel not seen in the model. This confirms the observation in section 4.2 that the model underpredicts the transport of freshwater from the North Channel of the Irish Sea around the coast of Scotland; a similar minimum is seen in the June climatology of sea surface salinity (Figure 6) but not the corresponding model results.

The model section continues as far as the Norwegian coast to demonstrate that the thermocline crosses the Norwegian Trench with little variation and that the model produces a complex salinity structure in the Norwegian Coastal current; the section is bisecting an anticyclonic baroclinic eddy apparent in the surface velocity field on this day. Unfortunately, there are not observations during the modeled period to assess these results.

6. Conclusions

By using AVHRR sea surface temperature measurements we have been able to make a synoptic assessment of this model prediction of SST over the whole domain. This shows the model accurately predicts the annual cycle of temperature and its large-scale spatial structure. The errors at the beginning and end of the model run do not differ greatly indicating that the model has good stability and is well suited for multiyear simulations. The results are generally more accurate on the shelf than in the northeast Atlantic, but the latter region is strongly influenced by the imposed temperature and salinity boundary conditions which are not in good agreement with the observations (Plates 1 and 2). These remotely sensed measurements provide an invaluable tool for model verification. However, they are less accurate than CTD observations, and there are important questions of their comparability with model results particularly in situations when the mixed layer is shallower than the near-surface vertical resolution of the model.

We have demonstrated that despite a significant increase in the number of degrees of freedom, this model reproduces the temperature structure of the whole of the northwest European continental shelf with a similar accuracy as the southern North Sea application of this model presented by *Holt and James* [1999b]; namely, typical errors in SST are $\sim$ 1°C in the winter and $\sim$ 1.5°C in the summer. The on-shelf CTD sections (Figures 8c and 8d) show the errors are also similar at depth. *Holt and James* [1999b] attributed the increase in errors in the temperature prediction in the summer to uncertainties in the modeling of the vertical temperature structure; particularly, in the estimation of vertical eddy diffusivities. Such is also the case here as questions raised in that paper on the modeling of vertical mixing in strongly stratified environments have yet to be addressed in the context of this model. Moreover, in this wider area model, a single value of the radiative attenuation coefficient (λ) is probably not sufficient; but an investigation of how this varies spatially and seasonally is beyond the scope of the present work.

We have not concentrated on the large CTD data set available in the southern North Sea during the period of the model run because to do so would draw our attention away from the model domain as a whole to focus a comparatively small area of it. However, if the analysis of the NSP CTD temperatures presented by *Holt and James* [1999b] is repeated with this shelf-wide model, we find that the overall rms error in the depth mean temperature has somewhat reduced (from 1.12° to 0.88°C) reflecting the higher resolution of the present model. However, the temperatures are now more significantly biased: the mean error in the depth mean temperature given by *Holt and James* [1999b] is -0.09°C compared with -0.25°C in the present work. This is due to the initial condition in the present paper not being set to match these particular observations (as was done in the southern North Sea model) and possibly because the advective heat flux is being over estimated (the surface forcing is identical in these two applications). The rms error in the depth varying component of the temperature is slightly greater in the shelf-wide model than the southern North Sea model (1.4°C compared with 1.3°C). This reflects the higher vertical resolution used here exaggerating the underestimation of diapycnal mixing noted above.

We have not been able to assess the salinity field produced by the model with the same rigor as the temperatures; however, a comparison with climatological values suggests the sea surface salinity is well modeled over much of the do-

main but identifies two areas of discrepancy: the Norwegian and Scottish Coastal Currents. The source of these errors requires further investigation, preferably with contemporary observations.

This model exists in a form suitable for massively parallel processing [*Proctor et al.*, 1999] and has been coupled to a complex ecological model (the European Regional Seas Ecosystem Model [*Allen et al.*, 2001]) which we plan to use with the extended northeast Atlantic domain described in section 1. The s coordinate transform allows the model to form a mixed layer, which crosses the shelf break and continues into deeper water with little variation. Since biological production is very sensitive to the vertical temperature and salinity structure, we suspect that the use of these coordinates will represent a significant improvement over the traditional σ coordinates in this planned coupled ocean-shelf ecosystem model.

Acknowledgments. This work was partially funded under a contract from the U.K. Meteorological Office (Met 1b/2670) and as part of the NERC LOIS integrated modeling phase (LOIS paper 828). Computer time was provided under a class 3 project from CSAR.

References

Allen, J. I., J. Blackford, J. T. Holt, R. Proctor, M. Ashworth, and J. Siddorn, A highly spatially resolved ecosystem model for the North West European Continental Shelf, *Sarsia*, in press, 2001.

Annan, J. D., Numerical methods for the solution of the turbulent energy equations in shelf seas, *Int. J. of Numer. Methods Fluids*, *29*, 193–206, 1999.

Annan, J. D., and J. C. Hargreaves, Sea surface temperature assimilation for a three-dimensional baroclinic model of shelf seas, *Cont. Shelf Res.*, *19*, 1507–1520, 1999.

Arakawa, A., Design of the UCLA general circulation model, *Tech. Rep. 7*, Univ. of Calif., Los Angeles, 1972.

Backhaus, J. O., and D. Hainbucher, A finite-difference general circulation model for shelf seas and its application to low frequency variability on the north European shelf, in *Three-Dimensional Models of Marine and Estuarine Dynamics*, *Oceanography Ser.*, vol. 45, edited by J. C. J. Nihoul and B. M. Jamart, pp. 221–244, Elsevier, New York, 1987.

Blumberg, A. F., and G. L. Mellor, A description of a three-dimensional coastal ocean model, in *Three Dimensional Coastal Ocean Models, Coastal and Estuarine Stud.*, vol. 4, edited by N. S. Heaps, pp. 1–16, AGU, Washington, D.C., 1987.

Charnock, H., K. R. Dyer, J. M. Huthnance, P. S. Liss, J. H. Simpson, and P. B. Tett (Eds.), *Understanding the North Sea System*, 222pp, Chapman and Hall, New York, 1994.

Colella, P., and P. R. Woodward, The piecewise parabolic method (ppm) for gas-dynamical simulations, *J. of Comput. Phys.*, *54*, 174–201, 1984.

Craig, P. D., and M. L. Banner, Modelling wave-enhanced turbulence in the ocean surface layer, *J. Phys. Oceanogr.*, *24*, 2546–2559, 1994.

de Kok, J. M., Baroclinic eddy formation in a Rhine plume model, *J. Mar. Syst.*, *12*, 35–52, 1997.

Deleersnijder, E., and P. Luyten, On the practical advantages of the quasi-equilibrium version of the Mellor and Yamada level 2.5 turbulence closure applied to numerical modelling, *Appl. Math. Modell.*, *18*, 281–287, 1994.

Flather, R. A., Results from a model of the northeast Atlantic relating to the Norwegian coastal current, in *The Norwegian Coastal Current*, vol. 2, edited by R. Saetre and M. Mork, pp. 427–458, Bergen Univ., Bergen, Norway, 1981.

Flather, R. A., R. Proctor, and J. Wolf, Oceanographic forecast models, in *Computer Modelling in the Environmental Sciences*, edited by D. G. Farmer and M. J. Rycroft, pp. 15–30, Clarendon, Oxford, England, 1991.

Galperin, B., L. H. Kantha, S. Hassid, and A. Rossati, A quasi-equilibrium turbulent energy model for geophysical flows, *J. Atmos. Sci.*, *45*, 55–62, 1988.

Gill, A. E., *Atmosphere-Ocean Dynamics*, Acedemic, San Diego, Calif., 1982.

Haney, R. L., On the pressure gradient force over steep topography in sigma coordinate models, *J. Phys. Oceanogr.*, *21*, 610–619, 1991.

Holt, J. T., and I. D. James, A simulation of the southern North Sea in comparison with measurements from the North Sea Project, part 2, Suspended particulate matter, *Cont. Shelf Res.*, *19*, 1617–1642, 1999a.

Holt, J. T., and I. D. James, A simulation of the southern North Sea in comparison with measurements from the North Sea Project, part 1, Temperature, *Cont. Shelf Res.*, *19*, 1087–1112, 1999b.

James, I. D., A front-resolving sigma coordinate model with a simple hybrid advection scheme, *Appl. Math. Modell.*, *10*, 87–92, 1986.

James, I. D., Advection schemes for shelf sea models, *J. Mar. Syst.*, *8*, 237–254, 1996.

James, I. D., A numerical model of the development of anticyclonic circulation in a gulf-type region of freshwater influence, *Cont. Shelf Res.*, *17*, 1803–1816, 1997.

Killworth, P. D., D. Stainforth, D. J. Webb, and S. M. Paterson, The development of a free-surface Bryan-Cox-Semtner ocean model, *J. Phys. Oceanogr.*, *21*, 1333–1348, 1991.

Kwong, S. C. M., A. M. Davies, and R. A. Flather, A three-dimensional model of the principal tides of the European shelf, *Prog. Oceanogr.*, *39*, 205–262, 1997.

Mellor, G. L., Retrospective on oceanic boundary layer modelling and second moment closure, in *The Parameterisation of Small Scale Processes: Proceedings of the Aha Hulikoa Hawaiian Winter Workshop*, edited by D. Henderson and P. Muller, pp. 251–271, Univ. of Hawaii, Manoa, 1989.

Mellor, G. L., An equation of state for numerical models of oceans and estuaries, *J. Atmos. Oceanic Technol.*, *8*, 609–611, 1991.

Mellor, G. L., and T. Yamada, A heirarchy of turbulence closure models for planetary boundary layers, *J. Atmos. Sci.*, *31*, 1791–1806, 1974.

Mellor, G. L., T. Ezer, and L.-Y. Oey, The pressure gradient conundrum of sigma coordinate ocean models, *J. Atmos. Oceanic Technol.*, *11*, 1126–1134, 1994.

Oey, L.-Y., Eddy energetics in the Faeroe-Shetland channel: A model resolution study, *Cont. Shelf Res.*, *17*, 1929–1944, 1997.

Oey, L.-Y., and P. Chen, A nested-grid ocean model: With application to the simulation of meanders and eddies in the Norwegian coastal current, *J. Geophys. Res.*, *97*(C12), 20,063–20,086, 1992a.

Oey, L.-Y. and P. Chen, A model simulation of circulation in the North Atlantic shelves and seas, *J. Geophys. Res.*, *97*(C12), 20,087–20,115, 1992b.

Pohlmann, T., Predicting the thermocline in a circulation model of the North Sea, part 1, Model description, calibration and verification, *Cont. Shelf Res.*, *16*, 131–146, 1996.

Proctor, R., and I. D. James, A fine-resolution 3D model of the southern North Sea, *J. Mar. Syst.*, *8*, 285–295, 1996.

Proctor, R., P. Lockey, and I. D. James, Development of portable self sea models for massively parallel machines, in *High Performance Computing*, edited by R. J. Allan et al., pp. 359–364, Kluwer Acad., New York, 1999.

Schlichtholz, P., and A. Jankowski, Hydrological regime and water

volume transport in the Faeroe-Shetland channel in summer of 1988 and 1989, *Oceanol. Acta, 16*(1), 11–22, 1993.

Schrum, C., Thermohaline stratification and instability at tidal mixing fronts: Results of an eddy resolving model of the German Bight, *Cont. Shelf Res., 17*, 689-716, 1997.

Simpson, J. H., and J. R. Hunter, Fronts in the Irish Sea, *Nature, 250*, 404–406, 1974.

Slørdal, L. H., The pressure gradient force in sigma-coordinate ocean models, *Int. J. Numer. Methods Fluids, 24*, 987–1017, 1997.

Smith, S. D., and E. G. Banke, Variation of the sea surface drag coefficient with wind speed, *Q. J. R. Meteorol Soc., 101*, 665–673, 1975.

Song, Y., and D. Haidvogel, A semi-implicit ocean circulation model using a generalized topography-following coordinate system, *J. Comput. Phys., 115* , 228–244, 1994.

Stelling, G. S., and J. A. T. M. van Kester, On the approximation of horizontal gradients in sigma co-ordinates for bathymetry with steep bottom slopes, *Int. J. Numer. Methods Fluids, 18*, 915–935, 1994.

Xing, J., and A. M. Davis, The influence of mixing length formulation and stratification upon tidal currents in shallow seas, *Estuarine Coastal Shelf Sci., 42*, 417–456, 1996.

J. T. Holt and I. D. James, Proudman Oceanographic Laboratory, Bidston Observatory, Birkenhead, CH43 7RA, U.K. (jholt@pol.ac.uk; idj@pol.ac.uk)

(Received March 31, 2000; revised November 22, 2000; accepted December 18, 2000.)